Technical article

Electromagnetic Broad Band Modeling Using a 3D Volume Integral Equation

Abstract — **In this paper, we describe a volume integral equation method for the numerical solution of the electromagnetic scattering from electrically anisotropic inhomogeneous objects. The unknown of the problem, defined as the sum of the conduction and polarization current densities, is decomposed in terms of its loop, star and facet components. The uniqueness of the corresponding discrete representation is enforced by suitable strategies also based on simple topological approaches. Furthermore, a convenient scaling of the unknowns is introduced in order to avoid the low frequency breakdown problem, showing its stability regardless of the operating frequency. This approach has been extensively validated by analyzing the resonant frequencies of classic split-ring resonators and the scattering from a uniaxial dielectric slab. A part of this paper is reproduced from an article recently published on IEEE Transactions on Antennas and Propagation [©2017 IEEE. Reprinted, with permission, from [8]].**

I Introduction

In many fields of application, the basic element for building complex models is the circuital component. It is well known, that the ideal circuit elements are connected trough their terminals and should respect the Kirchhoff laws, based on the topological constraints imposed by their connections. In this frame, the rigorous definition of the circuit parameters and the validity of the Kirchhoff laws can take place only at zero frequency, when the electric and magnetic fields in Maxwell equations decouple. The possibility of dealing with circuital models is of paramount importance and since a long time it has been a fundamental step in the numerical modeling of complex electromagnetic structures. Usually, the basic step for obtaining the circuit model is the subdivision of the device in several finite volume and surface elements, where the current and the surface charges are imposed to be distributed according to some elementary rules, uniformly distributed the most part of the time, so that partial resistances, self and mutual inductances and capacitance can be defined and linked together and to the sources through the application of the Kirchhoff laws. This "partial-element-equivalent-circuit (PEEC) technique" was firstly introduced by Ruheli in [1] and then widely used and improved in all these years by many researchers, mainly involved in the design of high speed interconnects [2] . Another important area of application where the electroquasistatic and magnetoquasistatic models cohesist leading to important resonant effects that can be efficiently taken into account by suitable LC equivalent circuits is represented by the design of metamaterials. In these materials it is possible to show tat there are particular conditions where the real part of the dielectric permittivity and/or the magnetic permeability becomes negative in a specific range of frequencies. For example, several studies have been devoted to a better understanding and the improvement of the $\mu-$negative behaviour of split-ring inclusions. Since, in this case, the dimensions of the constitutive cell are smaller than the operating wavelength, a quasi static approach is well suited for modeling their interaction with the electromagnetic fields by means of suitable equivalent circuits made of inductances and capacitances. However, these circuit parameters are usually found by means of suitable ad hoc assumptions on the behaviour of the current density patterns [3]. Other important effects arising in the electromagnetic modeling of metamaterials are related to their anisotropic properties. Specifically, the homogenization of metamaterials frequently returns effective anisotropic media. For instance, hyperbolic metamaterials are anisotropic, with one of the principal components of their electric susceptibility tensor being opposite in sign to the other two components [4]. Moreover, in 2006, Pendry et al. [5] and Leonhardt [6] showed how to accurately control the electromagnetic fields by properly design artificial materials. In particular, the general rules they provided to design metamaterial cloaks require the use of anisotropic and inhomogeneous material. Plasmon resonances in anisotropic nanoparticles also display very interesting features [7].

Various techniques are already available for efficiently handling anisotropic materials. A brief presentation of the advantages and limits of the more widespread approaches is done in [8] and will be here shortly recalled.

In the frame of the analytical and semi-analytical approaches, in 2002, Kiselev et al. [9] proposed the solution of the problem of scattering by arbitrarily-shaped homogeneous objects with radial and uniaxial anisotropy in the framework of the so called null field method (NFM). Unfortunately, the null field approach notoriously breaks down for very elongated or flattened particles [10].

With reference to a classic numerical method, we recall that Taflove et al. [11, 12, 13] first applied the finite-difference time domain method (FDTD) to anisotropic materials with diagonal permittivity or permeability tensors while in 1993, Schneider et al. [14] further extended the FDTD to also include nondiagonal tensors. Although differential formulations can surely benefit from the occurrence of sparse matrices, they require the discretization not only of the spatial region occupied by the scatterers but also of the embedding media. In addition, the numerical dispersion of the algorithm, spurious reflections at the PML interface, and staircase effects may deteriorate the accuracy of this method [15].

Instead, integral formulations appear to be particularly attractive since the spatial domain external to the scatterers does not need to be discretized, whereas the radiation conditions at infinity are naturally satisfied. In 2008, Mumcu et al. [16] extended the Poggio-Miller-Chang-Harrington-Wu-Tsai (PMCHWT) Surface Integral Equation (SIE) formulation to arbitrarily-shaped homogeneous uniaxial materials and solved it using the method of moments (MoM). The advantage of the SIE approach is that the unknowns are only localized on scatterers' boundary.

However, SIE methods can only treat piecewise homogeneous objects, while the Volume Integral Equation (VIE) approaches, despite requiring the discretization of the entire volume occupied by the scatterer, do not have this limitation. Different volume in-

tegral equation (VIE) approaches have been proposed so far to address the scattering problem from anisotropic media. Graglia and Uslenghi pioneered the use of VIE with a series of papers on the scattering from anisotropic objects [17, 18, 19]. Varadan et al. in 1989 [20] and Lakhtakia [21] in 1992 extended the Discrete Dipole Approximation (DDA) method to materials exhibiting uniaxial and biaxial anisotropy, respectively, approximating the scatter by a Cartesian array of polarizable point dipoles, each of them characterized by a polarizability tensor, [22]. Unfortunately, the DDA suffers from a high computational burden when large object are involved, and limited near-field accuracy. In addition, Draine and Flatau empirically demonstrated that the applicability of their approach is limited to materials whose refractive index is not large compared to unity [22]. More recently, Kobidze and Shanker derived a set of VIEs via the volume equivalence theorem and solved them numerically using the method of moments in combination with a fast multipole scheme [23]. Other approaches based on the implementation of a set of VIEs include the formulation proposed by Markkanen et al. [24], by Tong et al. [25] and by L. E. Sun [26], [27]. All these examples motivate the need of new and flexible computational tools for the efficient modeling of materials and devices in a broad band of frequencies, with a specific attention to the range going from static to quasi-static to full wave regimes. For the reasons outlined above, the integral formulations appear to be particularly attractive. Moreover, coupling to the circuit equations does not present particular difficulties ad the elements of the relevant matrices after discretization often can be directly used as parameters of equivalent RLC circuits.

The layout of the paper is as follows. The mathematical model and the numerical formulation are discussed in Sec. II. Then, Sec. III is devoted to introduce the numerical discretization of the unknowns in terms of the star, loop, and facet shape functions. Methods for ensuring the uniqueness of the representation will be also summarized, following [8]. In this section, we provide the explicit expression of the matrix equations together with the implemented strategies to overcome the low-frequency breakdown problem.

In Sec. IV we validate our numerical approach against experimental results and against the null field method for non-spherical scatterers. In particular, we investigate the scattering by a classic split-ring resonator and by a uniaxial anisotropic slab with two different aspect ratio. Finally, we prove the stability of our method over a broad range of frequencies by considering the test case of a slab with an assigned conductivity tensor, proving the condition number to be almost independent of the frequency.

II Mathematical Model and Numerical Formulation of the Field Problem

Let us consider an anisotropic and inhomogeneous material occupying a volume Ω, which is bounded by a closed surface $\partial\Omega$. We also assume the material to be non-magnetic and spatially non-dispersive. The material is characterized by a relative permittivity tensor $\bar{\varepsilon}_r$, and a conductivity tensor $\bar{\sigma}$, which may be functions of the position. We assume that the material properties may show abrupt discontinuities, appearing on the interfaces of material regions $\Omega_1, \ldots, \Omega_N$, as shown in Fig. 1(a). We denote with Σ the union of the surfaces where the material properties have a jump, i.e. $(\Sigma = \partial\Omega_1 \cup \ldots \cup \partial\Omega_N)$. The object is excited by a monochromatic electromagnetic field incoming from infinity.

We consider as unknown of the problem the generalized current density in the material region, namely the sum of the conduction current density and the polarization current density:

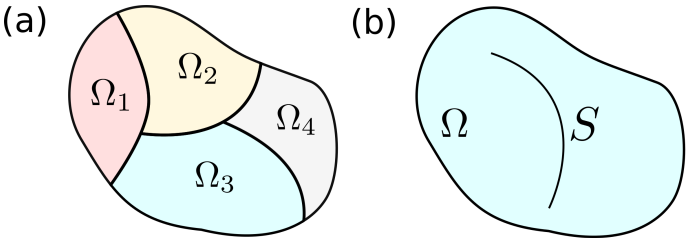

Figure 1: (a) Abrupt discontinuities of the material properties appear on the boundary of each subdomain, which is a closed surface. (b) Abrupt discontinuity of the material properties appears on S which is not a closed surface.©2017 IEEE. Reprinted, with permission, from [8].

$$\mathbf{J}(\mathbf{r}) = \begin{cases} (\bar{\sigma}(\mathbf{r}) + j\omega\bar{\chi}(\mathbf{r})\varepsilon_0)(\mathbf{E}(\mathbf{r}) + \mathbf{E}_0(\mathbf{r})) \text{ in } \Omega\backslash\Sigma \\ \mathbf{0} \text{ in } \mathbb{R}^3\backslash\Omega \end{cases} \tag{1}$$

where $\mathbf{E}(\mathbf{r})$ is the scattered electric field, $\mathbf{E}_0(\mathbf{r})$ is the incident electric field, $\bar{\chi}$ the dielectric susceptibility and ε_0 is the free space dielectric constant. [28, 29, 31].

It is important for what follows to recall that Surface charges ρ_S may arise on abrupt discontinuities of the material properties. On the other hand, volumetric charges ρ_V may arise when the material properties are graded or anisotropic. These charges are governed by the equations:

$$\nabla \cdot \mathbf{E} = \frac{1}{\varepsilon_0}\rho_V \qquad \text{in } \Omega\backslash\Sigma, \tag{2}$$

$$[\mathbf{E} \cdot \hat{\mathbf{n}}] = \frac{1}{\varepsilon_0}\rho_S \qquad \text{on } \Sigma, \tag{3}$$

where $[\mathbf{A} \cdot \hat{\mathbf{n}}]$ denotes the jump of the normal component of $\mathbf{A}$, that is $[\mathbf{A} \cdot \hat{\mathbf{n}}] = \mathbf{A}_i \cdot \hat{\mathbf{n}}_i + \mathbf{A}_k \cdot \hat{\mathbf{n}}_k$ on points at the interface between regions Ω_i and Ω_k and $\hat{\mathbf{n}}_i$ $(\hat{\mathbf{n}}_k)$ points outward from region Ω_i (Ω_k).

A Loop-Star-Facet (LSF) decomposition

At zero frequency the electric and magnetic fields in Maxwell equations decouple. In particular, the solenoidal component $\mathbf{J}^S$ of the current density produces a magnetic field while the non-solenoidal component produces an electric field. Notice that, in order to have a physically finite charge $\rho_V = -\nabla \cdot \mathbf{J}/j\omega$ as $\omega \to 0$, the non-solenoidal current density should vanish with ω linearly as $\omega \to 0$. Therefore, the main numerical problem at low frequencies is to correctly reproduce the different scaling with the frequency of the field. The so called low frequency breakdown [30] [31] is due to this different scaling with ω of the solenoidal and non-solenoidal component of the current density as tends to zero. This behavior should be carefully numerically modeled, by representing the unknown as the sum of its solenoidal and non-solenoidal components. The separation in two distinct components allows to avoid the ill-conditioning of the relevant stiffness matrix at low frequencies by properly scaling, at a given frequency, the solenoidal component with respect to the non-solenoidal component. As a consequence it is possible to model accurately and consistently the interactions between the magneto-quasistatic (MQS) part of the solution, leading to the inductance and resistance contributions to the input impedance, and the electro-quasistatic (EQS) model accounting for the capacitance and conductance contribution.

Following [31], we define the following functional spaces:

$$\mathcal{J}_L = \{\mathbf{w} \in H(\mathrm{div}, \Omega) \,|\nabla \cdot \mathbf{w} = 0 \text{ in } \Omega,\, \mathbf{w} \cdot \hat{\mathbf{n}} = 0 \text{ on } \partial\Omega\}$$
$$\mathcal{J}_S = \{\mathbf{w} \in H(\mathrm{div}, \Omega\backslash\Sigma) \,|\nabla \cdot \mathbf{w} = 0 \text{ in } \Omega\backslash\Sigma\}$$
$$\mathcal{J}_F = \{\mathbf{w} \in H(\mathrm{div}, \Omega) \,|\, \mathbf{w} \cdot \hat{\mathbf{n}} = 0 \text{ on } \partial\Omega\}\,.$$

They are the natural functional spaces for splitting the current density $\mathbf{J}$ into the sum of its loop, star, and facet components, denoted by $\mathbf{J}_L$, $\mathbf{J}_S$, and $\mathbf{J}_F$, respectively, namely:

$$\mathbf{J} = \mathbf{J}_L + \mathbf{J}_S + \mathbf{J}_F, \tag{4}$$

where $\mathbf{J}_L \in \mathcal{J}_L$, $\mathbf{J}_S \in \mathcal{J}_S$ and $\mathbf{J}_F \in \mathcal{J}_F$.

In this way, the surface and volume charge density are directly derived from the components $\mathbf{J}_S$ and $\mathbf{J}_F$, respectively:

$$\rho_V = -\frac{1}{j\omega}\nabla \cdot \mathbf{J}_F \text{ in } \Omega$$
$$\rho_S = \frac{1}{j\omega}\left[\mathbf{J}_S \cdot \hat{\mathbf{n}}\right] \text{ on } \Sigma.$$

It is worth noting that spaces $\mathcal{J}_L$, $\mathcal{J}_S$ and $\mathcal{J}_F$ have non trivial intersection. For instance, $\mathcal{J}_L \subset \mathcal{J}_S$ and $\mathcal{J}_L \subset \mathcal{J}_F$. This means that decomposition (4) is not unique. Uniqueness of such decomposition will be enforced at discrete level in the following sections.

B The integral equation

We express the scattered electric field $\mathbf{E}$ in terms of the vector and scalar potentials $\mathbf{A}$ and φ, namely $\mathbf{E} = -j\omega\mathbf{A} - \nabla\varphi$ assuming the Lorenz gauge, i.e. $\nabla \cdot \mathbf{A} + j\omega\varepsilon_0\mu_0\varphi = 0$. The vector and scalar potentials can be directly obtained from the current density $\mathbf{J}$ and from the surface and volume charge densities ρ_V and ρ_S through the scalar free space Green function $g(\mathbf{r}, \omega) \triangleq e^{-jkr}/(4\pi r)$:

$$\mathbf{A}(\mathbf{r}, \omega) = \mu_0 \int_\Omega \mathbf{J}(\mathbf{r}')\, g(\mathbf{r} - \mathbf{r}', \omega)\, \mathrm{d}V', \tag{5}$$

$$\varphi(\mathbf{r}, \omega) = \frac{1}{j\omega\varepsilon_0}\int_\Sigma \left[\mathbf{J}_S \cdot \hat{\mathbf{n}}\right](\mathbf{r}')\, g(\mathbf{r} - \mathbf{r}', \omega)\, \mathrm{d}S' - \frac{1}{j\omega\varepsilon_0}\int_\Omega \nabla \cdot \mathbf{J}_F(\mathbf{r}')\, g(\mathbf{r} - \mathbf{r}', \omega)\, \mathrm{d}V'. \tag{6}$$

By combining $\mathbf{E} = -j\omega\mathbf{A} - \nabla\varphi$ together with (1), (5) and (6) we obtain the integral equation in terms of the unknown $\mathbf{J}$:

$$\left(\bar{\sigma} + j\omega\bar{\chi}\varepsilon_0\right)^{-1}\mathbf{J}(\mathbf{r}) + j\omega\mu_0\int_\Omega \mathbf{J}(\mathbf{r}')\, g(\mathbf{r} - \mathbf{r}', \omega)\, \mathrm{d}V' + \frac{1}{j\omega\varepsilon_0}\nabla\int_\Sigma \left[\mathbf{J}_S \cdot \hat{\mathbf{n}}\right](\mathbf{r}')\, g(\mathbf{r} - \mathbf{r}', \omega)\, \mathrm{d}S' - \frac{1}{j\omega\varepsilon_0}\nabla\int_\Omega \nabla\cdot\mathbf{J}_F(\mathbf{r}')\, g(\mathbf{r} - \mathbf{r}', \omega)\, \mathrm{d}S' = \mathbf{E}_0(\mathbf{r}) \quad \forall \mathbf{r} \in \Omega. \tag{7}$$

III Numerical model

A Discretization of the unknowns

In order to obtain the numerical discretization of Eq. 7, we introduce a finite-dimensional approximation of the currents $\mathbf{J}_L$, $\mathbf{J}_S$ and $\mathbf{J}_F$ in terms of linear combinations of suitable shape functions, denoted as $\mathbf{w}_k^L$'s, $\mathbf{w}_k^S$'s and $\mathbf{w}_k^F$'s, respectively.

The $\mathbf{w}_k^L$'s are the shape functions used to discretize the loop component $\mathbf{J}_L$. Each function $\mathbf{w}_k^L$ is associated to the k-th edge of the finite element discretization of the volume Ω and it is defined as the curl of the k-th edge-element shape functions $\mathbf{N}_k$:

$$\mathbf{w}_k^L(\mathbf{r}) = \nabla \times \mathbf{N}_k(\mathbf{r})$$

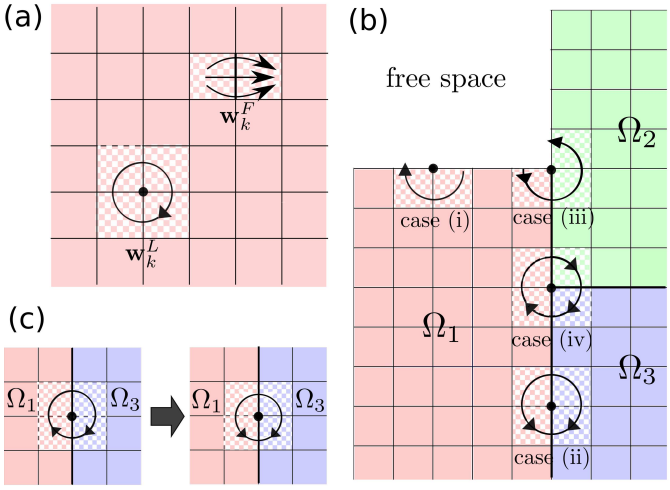

Figure 2: (a) Typical current density distribution for a loop shape function (L-type) and a facet shape function (F-type). (b) Different types of star-shape functions. The dots represent the trace of the edges to which the shape functions are associated to. Regions with different hatch represent different shape functions. For instance, there are two shape functions for Case (iii) and three shape functions for case (iv). (c) The process for deriving a star-type shape function from the curl of an edge element shape function. The support of each shape function is represented with a checkerboard. ©2017 IEEE. Reprinted, with permission, from [8].

In Fig. 2 (a) we sketch the typical current density distribution of a loop shape function.

The $\mathbf{w}_k^S$'s are the shape functions employed to discretize the star component $\mathbf{J}_S$ and are therefore devoted to model the surface charge density ρ_S appearing on abrupt discontinuities. Thus, we associate the $\mathbf{w}_k^S$'s to the edges belonging to the surface Σ where the material discontinuity takes place. The definition of the $\mathbf{w}_k^S$'s changes depending on whenever the associated edge belongs to the interface between (i) a material region and the free-space, (ii) two different material regions, (iii) two or more material regions and the free-space, and (iv) three or more material regions. These scenarios are exemplified in Figure 2 (b), where the k- edge to which the star shape function is associated is represented with a dot, being orthogonal to the page's plane. In particular, in the case (ii), the $\mathbf{w}_k^S$ is defined as the curl of k-th edge-element shape function provided that its sign is changed in one and only one of the two material regions, as showed in Figure 2 (c). In the remaining three scenarios the $\mathbf{w}_k^S$'s are defined as the restriction of the curl of k-the edge element shape function to specific material region under consideration.

The $\mathbf{w}_k^F$'s are the shape functions used to discretize the facet component $\mathbf{J}_F$ and are devoted to model the volumetric charge density ρ_V appearing in Ω. The $\mathbf{w}_k^F$'s are the usual facet shape functions, the corresponding DoF are related to the facets of the mesh [32], [33]. The typical current density distribution featured by $\mathbf{w}_k^F$ is sketched in Figure 2 (a).

In conclusion, the unknown current density distribution is represented, at the discrete level, as

$$\mathbf{J} = \sum_{k=1}^{N_L} I_k^L \mathbf{w}_k^L + \sum_{k=1}^{N_S} I_k^S \mathbf{w}_k^S + \sum_{k=1}^{N_F} I_k^F \mathbf{w}_k^F \tag{8}$$

where the coefficients I_k^L's, I_k^S's, and I_k^F's are the degrees of freedom (DoFs) for the loop, star and facet components, while N_L, N_S and N_F are the number of loop, star and facet involved in the discretization.

A1. Uniqueness of the representation

Let $\mathcal{W}_L$, $\mathcal{W}_S$ and $\mathcal{W}_F$ be the finite-dimensional linear spaces of the current density distributions generated by the loop, star and facet shape functions. In particular, $\mathcal{W}_L$ is spanned by the shape functions associated to the edges of the mesh of Ω, $\mathcal{W}_S$ is spanned by the shape functions associated to the edges lying on Σ, and $\mathcal{W}_F$ is spanned the functions associated to the internal facets of the mesh of Ω. This (preliminary) choice does not guarantee the uniqueness of the representation for each individual component $\mathbf{J}_L$, $\mathbf{J}_S$ and $\mathbf{J}_F$. Here we first focus on the uniqueness of the representation for each individual components and, then, on their sum $\mathbf{J} = \mathbf{J}_L + \mathbf{J}_S + \mathbf{J}_F$.

Uniqueness for the loop component has been treated long ago in [28], [29].

Uniqueness for the star component was enforced in [31] and successively in [34] by means of topological algorithms. Here, we propose an alternative method which leads to a simpler implementation. First, we note that if two different sets of DoFs, e.g. a_k's and b_k's, represent the same $\mathbf{J}_S$, then $\sum_k (a_k - b_k)\, \mathbf{w}_k^S$ is vanishing and it is therefore associated to a solenoidal current density distribution (the trivial one). Thus, the uniqueness can be enforced by preventing the DoFs to generate solenoidal distributions. Then, we consider the matrix mapping the DoFs into the net charge on each individual facet of Σ. Specifically, from [31] we have that

$$\mathbf{q}^S = \frac{1}{j\omega} \mathbf{P}^S \mathbf{I}^S,$$

where $\mathbf{q}^S$ is the column vector of the net charge on each individual facet Σ_i of Σ, $\mathbf{I}^S$ is the column vector associated to the DoFs of the star component and

$$P_{ij}^S = \int_{\Sigma_i} \mathbf{w}_j^S \cdot \hat{\mathbf{n}} \mathrm{d}S, \ \forall i = 1, ..., N_\Sigma \ \forall j = 1, ..., N_S$$

Solenoidal current density distributions correspond to vanishing $\mathbf{q}^S$. Thus, to remove these component we need to discard the DoFs belonging to the null space of the matrix $\mathbf{P}^S$, which can be done by Gaussian elimination. In particular, the DoFs associated to nonsolenoidal current density distributions are associated the nonvanishing columns of $\mathbf{P}^S$ after Gaussian elimination. Since the matrix $\mathbf{P}^S$ consists of integer entries, the Gaussian elimination can be made immune to roundoff errors which, otherwise, could affect the final results.

Likewise, the uniqueness for the facet shape functions representation can be imposed by considering that

$$\mathbf{q}^V = -\frac{1}{j\omega} \mathbf{P}^V \mathbf{I}^V,$$

where $\mathbf{q}^V$ is the column vector of the net charge in each element of the mesh discretizing Ω, $\mathbf{I}^V$ is the column vector associated to the facet DoFs, and

$$P_{ij}^V = \int_{\partial V_i} \mathbf{w}_j^F \cdot \hat{\mathbf{n}} \mathrm{d}S, \ \forall i = 1, ..., N \ \forall j = 1, ..., N_F$$

where ∂V_i is the boundary of the $i-$th element of the finite element mesh, $\hat{\mathbf{n}}$ its outward normal vector and N the number of elements of the mesh. As for the star shape functions, the DoFs representing solenoidal current densities belong to the null space of the integer matrix $\mathbf{P}^V$, therefore their occurrence can be prevented by Gaussian elimination.

Uniqueness of the representation for the facet shape functions can be also imposed by a simple topological approach [8] similar to that proposed in [34] for the star shape functions.

Once the uniqueness of the representation of each single $\mathbf{J}$ component (loop, star and facet) has been enforced, we obtain as a byproduct also the uniqueness of their mutual combination, described by Eq. 8. We prove this argument by reductio ad absurdum. If the shape functions are not linearly independent, the loop component, i.e. the first term in Eq. 8, can be represented as linear combination of the star and facet components. But this is impossible because star and facet components cannot generate a solenoidal current density. Similar argument for the other two case: a star component cannot be represented as sum of loop and facets components, a facet component cannot be represented as the sum of a loop and star component.

B Discrete model

The discrete model, that we numerically solve in the next section, is obtained by substituting the representation (8) into the integral equation (7) and applying the Galerkin method projecting along the loop, star, and facet shape functions. Following the outlined steps, we obtain the linear problem:

$$\mathbf{Z}\mathbf{I} = \mathbf{V}, \tag{9}$$

being

$$\mathbf{Z} = \mathbf{R} + j\omega\mathbf{L} + \frac{1}{j\omega}\mathbf{D}, \tag{10}$$

where we have defined the block matrices

$$\mathbf{R}(\omega) = \begin{bmatrix} \mathbf{R}_{LL} & \mathbf{R}_{LS} & \mathbf{R}_{LF} \\ \mathbf{R}_{SL} & \mathbf{R}_{SS} & \mathbf{R}_{SF} \\ \mathbf{R}_{FL} & \mathbf{R}_{FS} & \mathbf{R}_{FF} \end{bmatrix}, \tag{11}$$

$$\mathbf{L}(\omega) = \begin{bmatrix} \mathbf{L}_{LL} & \mathbf{L}_{LS} & \mathbf{L}_{LF} \\ \mathbf{L}_{SL} & \mathbf{L}_{SS} & \mathbf{L}_{SF} \\ \mathbf{L}_{FL} & \mathbf{L}_{FS} & \mathbf{L}_{FF} \end{bmatrix}, \tag{12}$$

$$\mathbf{D}(\omega) = \begin{bmatrix} \mathbf{0} & \mathbf{0} & \mathbf{0} \\ \mathbf{0} & \mathbf{D}_{SS} & \mathbf{D}_{SF} \\ \mathbf{0} & \mathbf{D}_{FS} & \mathbf{D}_{FF} \end{bmatrix}, \tag{13}$$

and the block vectors:

$$\mathbf{V}(\omega) = \begin{bmatrix} \mathbf{V}^L \\ \mathbf{V}^S \\ \mathbf{V}^F \end{bmatrix}, \qquad \mathbf{I} = \begin{bmatrix} \mathbf{I}^L \\ \mathbf{I}^S \\ \mathbf{I}^F \end{bmatrix}.$$

First, let us explicitly derive the elements of the matrix $\mathbf{D}$, which are the Galerkin discretization of the last two terms on the l.h.s. of Eq. 7 representing the reaction scalar potential, i.e. $\varphi_R(\mathbf{r}, \omega) = \varphi_R^S(\mathbf{r}, \omega) + \varphi_R^F(\mathbf{r}, \omega)$ where

$$\varphi_R^S(\mathbf{r}, \omega) = \frac{1}{j\omega\varepsilon_0} \int_\Sigma [\mathbf{J}_S \cdot \hat{\mathbf{n}}](\mathbf{r}')\, g(\mathbf{r} - \mathbf{r}', \omega)\, \mathrm{d}S'$$

$$\varphi_R^F(\mathbf{r}, \omega) = -\frac{1}{j\omega\varepsilon_0} \int_\Omega \nabla \cdot \mathbf{J}_F(\mathbf{r}')\, g(\mathbf{r} - \mathbf{r}', \omega)\, \mathrm{d}V'.$$

We notice that $\varphi_R^S(\mathbf{r}, \omega)$ can be also written as follows:

$$\varphi_R^S(\mathbf{r}, \omega) = \frac{1}{j\omega\varepsilon_0} \sum_{k=1}^{N} \int_{\partial\Omega_k} (\mathbf{J}_S \cdot \hat{\mathbf{n}}_k)(\mathbf{r}')\, g(\mathbf{r} - \mathbf{r}', \omega)\, \mathrm{d}S',$$

being $\mathbf{J}_S$ evaluated on the internal page of $\partial\Omega_k$. In conclusion, the elements of the matrix $\mathbf{D}$ are:

$$\left(\mathbf{D}_{SS}\right)_{p,q} = \frac{1}{\varepsilon_0}\sum_{j,k=1}^{N}$$
$$\int_{\partial\Omega_k}\int_{\partial\Omega_j}\left(\mathbf{w}_q^S\cdot\hat{\mathbf{n}}_j\right)(\mathbf{r}')\left(\mathbf{w}_p^S\cdot\hat{\mathbf{n}}_k\right)(\mathbf{r})\,g\left(\mathbf{r}-\mathbf{r}',\omega\right)\mathrm{d}S'\mathrm{d}S$$
$$\left(\mathbf{D}_{FS}\right)_{p,q} = -\frac{1}{\varepsilon_0}\sum_{k=1}^{N}$$
$$\int_{\Omega}\int_{\partial\Omega_k}\left(\mathbf{w}_p^S\cdot\hat{\mathbf{n}}_k\right)(\mathbf{r}')\left(\nabla\cdot\mathbf{w}_q^F\right)(\mathbf{r})\,g\left(\mathbf{r}-\mathbf{r}',\omega\right)\mathrm{d}S'\mathrm{d}V$$
$$\left(\mathbf{D}_{FF}\right)_{p,q} =$$
$$\frac{1}{\varepsilon_0}\int_{\Omega}\int_{\Omega}\left(\nabla\cdot\mathbf{w}_p^F\right)(\mathbf{r})\left(\nabla\cdot\mathbf{w}_q^F\right)(\mathbf{r}')\,g\left(\mathbf{r}-\mathbf{r}',\omega\right)\mathrm{d}V'\mathrm{d}V$$
$$\mathbf{D}_{SF} = \mathbf{D}_{FS}^T.$$

The matrices $\mathbf{R}$ and $\mathbf{L}$ are associated to the first and second elements on the l.h.s. of Eq. 7, respectively. The generic occurrences of these matrices are:

$$\left(\mathbf{R}_{\alpha\beta}\right)_{pq} = \int_{\Omega}\mathbf{w}_p^{\alpha}\cdot\left(\bar{\sigma}+j\omega\varepsilon_0\bar{\chi}\right)^{-1}\mathbf{w}_q^{\beta}\mathrm{d}V$$
$$\left(\mathbf{L}_{\alpha\beta}\right)_{pq} = \mu_0\int_{\Omega}\int_{\Omega}\mathbf{w}_p^{\alpha}(\mathbf{r})\cdot\mathbf{w}_q^{\beta}(\mathbf{r}')\,g\left(\mathbf{r}-\mathbf{r}',\omega\right)\mathrm{d}V\mathrm{d}V'$$

$\forall\alpha,\beta\in\{L,S,F\}$. The element of the vector associated to the Galerkin discretization of the r.h.s. of Eq. 7 is:

$$\left(\mathbf{V}^{\alpha}\right)_p = \int_{\Omega}\mathbf{w}_p^{\alpha}\cdot\mathbf{E}_0\mathrm{d}V,\quad\forall\alpha\in\{L,S,F\}. \tag{14}$$

C Scaling

The discrete model outlined in the previous paragraphs, thanks to the loop-star-facet decomposition, provides an easy understanding of the low-frequency breakdown problem ([31], [30]). Specifically, if the conductivity tensor $\bar{\sigma}$ approaches a non-vanishing value for $\omega\to 0$ then, in the same *low frequency* limit, the matrix $\mathbf{Z}$ approaches the matrix

$$\mathbf{Z}_0 = \mathbf{R}+\frac{1}{j\omega}\begin{bmatrix}\mathbf{0} & \mathbf{0} & \mathbf{0}\\ \mathbf{0} & \mathbf{D}_{SS}^0 & \mathbf{D}_{SF}^0\\ \mathbf{0} & \mathbf{D}_{FS}^0 & \mathbf{D}_{FF}^0\end{bmatrix}, \tag{15}$$

being $\mathbf{D}_{\alpha\beta}^0$ a matrix whose elements are defined analogously to those of $\mathbf{D}_{\alpha\beta}$, provided that each occurrence of the dynamic Green function is replaced with the static one. The second term in (15) dominates the first term and makes $\mathbf{Z}_0$ singular. On the other hand, if $\bar{\sigma}$ approaches a vanishing value in the low frequency limit, the matrix $\mathbf{Z}$ approaches the non singular matrix[1]:

$$\mathbf{Z}_0 = \frac{1}{j\omega}\begin{bmatrix}\mathbf{Q}_{LL} & \mathbf{Q}_{LS} & \mathbf{Q}_{LF}\\ \mathbf{Q}_{SL} & \mathbf{Q}_{SS}+\mathbf{D}_{SS}^0 & \mathbf{Q}_{SF}+\mathbf{D}_{SF}^0\\ \mathbf{Q}_{FL} & \mathbf{Q}_{FS}+\mathbf{D}_{FS}^0 & \mathbf{Q}_{FF}+\mathbf{D}_{FF}^0\end{bmatrix},$$

where[2]

$$\left(\mathbf{Q}_{\alpha\beta}\right)_{pq} = \frac{1}{\varepsilon_0}\int_{\Omega}\mathbf{w}_p^{\alpha}\cdot\left(\bar{\chi}\right)^{-1}\mathbf{w}_q^{\beta}\mathrm{d}V.$$

To overcome the low-frequency breakdown problem a possible strategy is the scaling of the unknowns. This is an extremely simple but effective remedy which has been successfully used in past works ([30],[31]). Specifically, the idea is to introduce a scaled version of the unknowns:

$$\mathbf{I}^L = \tilde{\mathbf{I}}^L,\ \mathbf{I}^S = \alpha_S\tilde{\mathbf{I}}^S,\ \mathbf{I}^F = \alpha_F\tilde{\mathbf{I}}^F$$

so that the block matrices on the main diagonal, after scaling, have similar norms. Therefore, Eq. (9) is replaced by

$$\tilde{\mathbf{Z}}\tilde{\mathbf{I}} = \tilde{\mathbf{V}} \tag{16}$$

where

$$\tilde{\mathbf{Z}} = \begin{bmatrix}1 & 0 & 0\\ 0 & \alpha_S & 0\\ 0 & 0 & \alpha_F\end{bmatrix}\mathbf{Z}\begin{bmatrix}1 & 0 & 0\\ 0 & \alpha_S & 0\\ 0 & 0 & \alpha_F\end{bmatrix}, \tag{17}$$

$$\tilde{\mathbf{V}} = \begin{bmatrix}\mathbf{V}^L\\ \alpha_S\mathbf{V}^S\\ \alpha_F\mathbf{V}^F\end{bmatrix},\qquad \tilde{\mathbf{I}} = \begin{bmatrix}\tilde{\mathbf{I}}^L\\ \tilde{\mathbf{I}}^S\\ \tilde{\mathbf{I}}^F\end{bmatrix}.$$

Coefficient α_S and α_F are chosen so that $\|\mathbf{R}_{LL}+j\omega\mathbf{L}_{LL}\| = \alpha_S^2\left\|\mathbf{R}_{SS}+j\omega\mathbf{L}_{SS}+\frac{1}{j\omega}\mathbf{D}_{SS}\right\| = \alpha_F^2\left\|\mathbf{R}_{FF}+j\omega\mathbf{L}_{FF}+\frac{1}{j\omega}\mathbf{D}_{FF}\right\|$, where $\|\cdot\|$ is a suitable matrix norm. It is worth noting that, if σ approaches a non-vanishing value, we have $\alpha_S = O\left(\sqrt{\omega}\right)$ and $\alpha_F = O\left(\sqrt{\omega}\right)$ for $\omega\to 0$, otherwise $\alpha_S = O\left(1\right)$ and $\alpha_F = O\left(1\right)$.

We conclude this section by stressing out that the scaling has a tremendous effect on the condition number [31]. Numerical examples in the next sections will demonstrate the effectiveness of our scaling approach in transforming an almost singular discrete model into a well conditioned one.

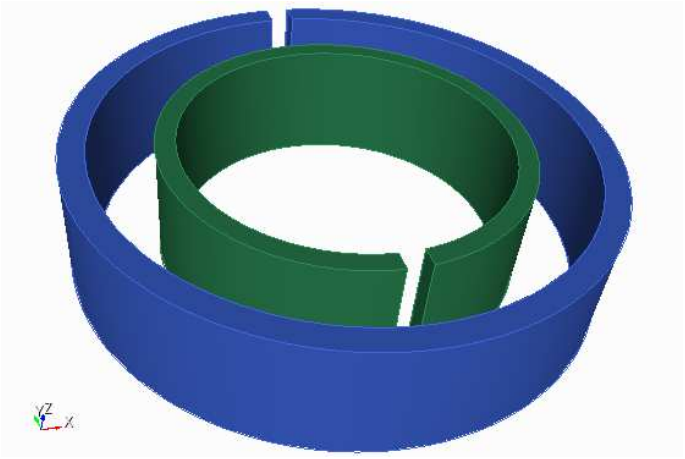

Figure 3: 3D view of the split ring here analyzed.

IV Numerical Results

In this section, we analyze several numerical examples for illustrating the main features of the computational method discussed in this paper. In particular, our three-dimensional volume integral formulation (VIE) is validated against experimental data and against the null field method in the presence of uniaxial dielectric objects [9], [10]. Finally, we provide numerical evidence of the stability of the presented VIE method over a broad range of frequencies.

[1] We need $\sigma = O\left(\omega\right)$ for $\omega\to 0$.

[2] We assume $\sigma/\omega\to 0$ for $\omega\to 0$. Minor modifications are required if σ/ω approaches a non vanishing values.

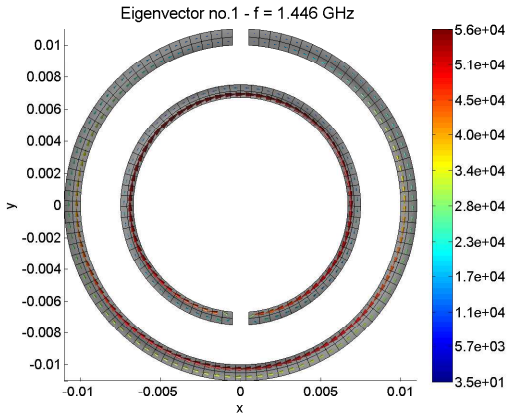

(a) Mode no. 1, xy view

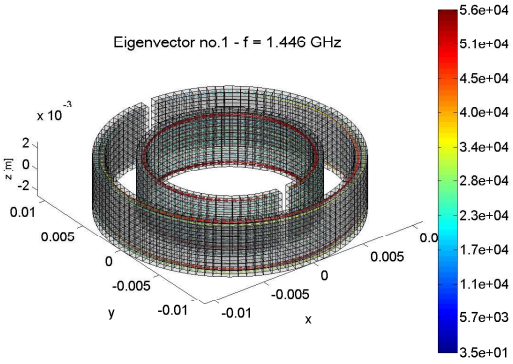

(b) Mode no. 1, $3D$ view

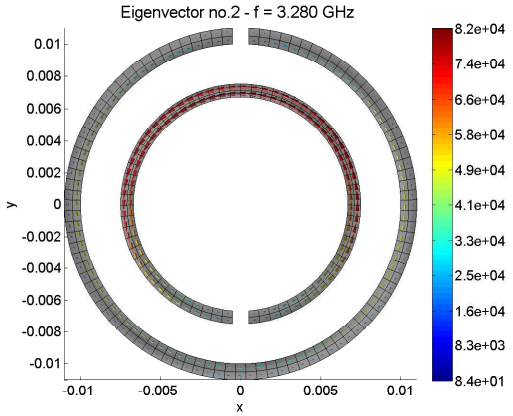

(c) Mode no. 2, xy view

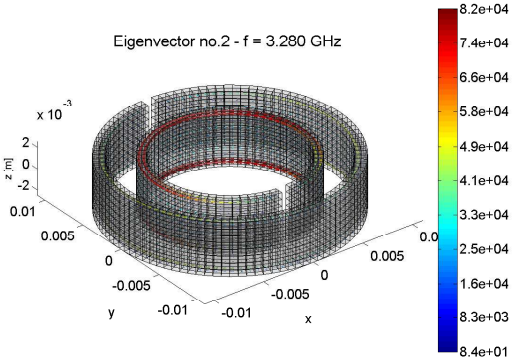

(d) Mode no. 2, $3D$ view

Figure 4: Mode 1-2. They have 2640 elements leading to $N_L = 3600$ loop shape functions and $N_S = 3362$ star shape functions.

A Split-ring resonators

The first example deals with the analysis of a resonant split-ring, shown in Fig. 3. This element was firstly proposed by Pendry *et al.* [35] that proposed a way to synthetize $\mu - negative$ features through these resonant loop inclusions.

The dimensions of these split-rings are smaller compared to the operating wavelength; consequently, the resonances can be easily obtained in the quasistatic limit, by taking into account the inductance as well as the capacitance effects. These represent unique features of the problem that can be conveniently analysed by means of a PEEC approach [2], or by introducing suitable surface approximation of the source distribution as done in [36]. However, in both cases, several simplifying assumptions have to be introduced limiting, at least in principle, the generality of these numerical models. In particular, 3D skin effects as well as anisotropic dielectric and conducting media could represent difficult problems when tackled with those approaches.

In the quasi-static limit with ideal conductors, the resonant frequencies can be obtained as the solution of the following gen-

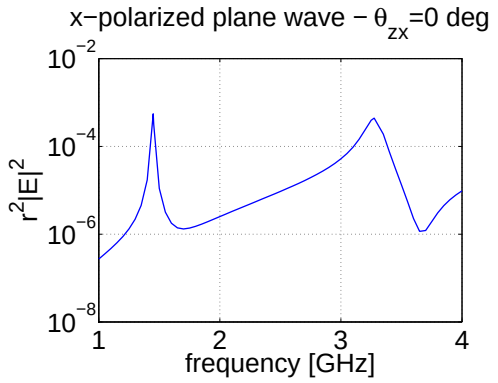

(a) $x-$polarized plane wave, propagating along the $y-$ axis

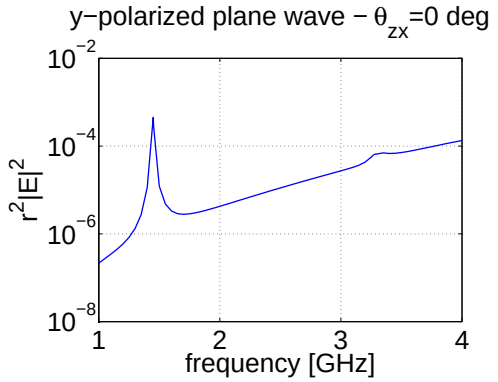

(b) $y-$polarized plane wave, propagating along the $x-$ axis

Figure 5: Squared magnitude of the electric field scattered from the slit-ring with $l = 5mm, r_{e1} = 11mm, r_{i1} = 10mm, r_{e2} = 7.5mm, r_{i2} = 6.7mm$, and $g = 1mm$, evaluated in the far zone along the z axis as a function of the frequency.

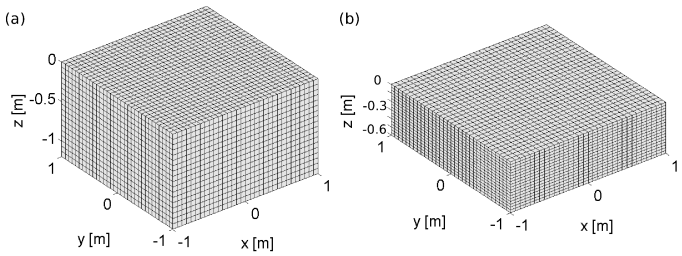

Figure 6: Mesh of the slab with height $H = 1.2m$ (a) and with $H = 0.6m$ (b) ©2017 IEEE. Reprinted, with permission, from [8].

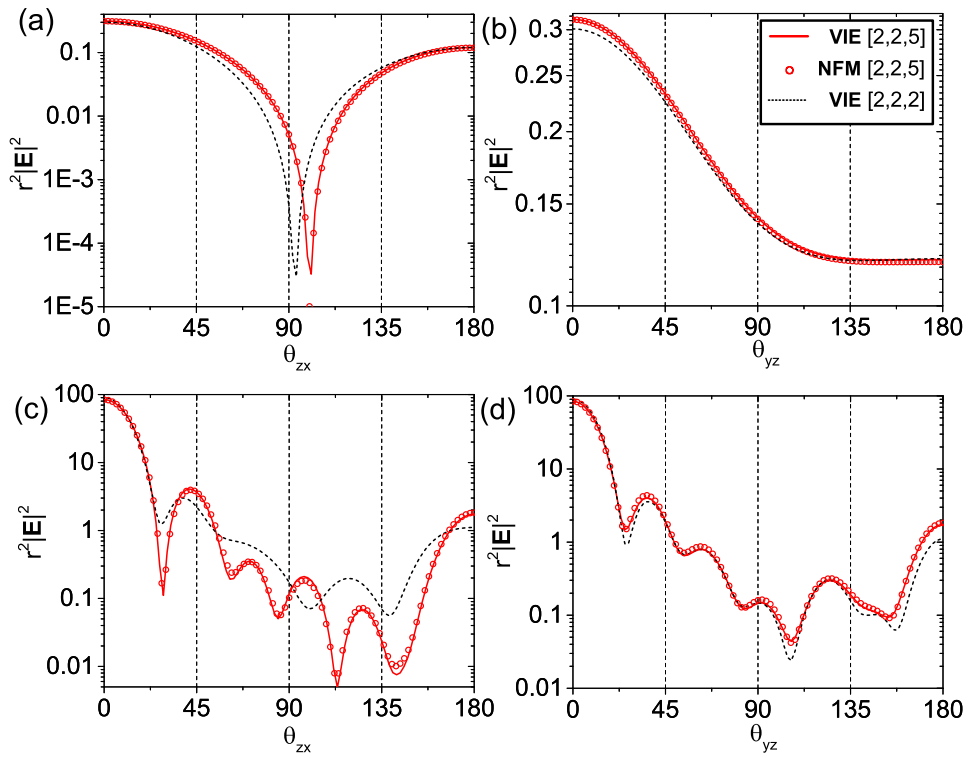

Figure 7: Squared magnitude of the electric field scattered from an anisotropic slab with equal length L and width W, i.e $L = W = 2m$, and height $H = 1.2m$ and with $\bar{\bar{\varepsilon}}_r = \text{diag}\,[2, 2, 5]$, evaluated in the far zone as a function of the inclination angle θ in zx plane (a),(c) and in the yz plane (b),(d). The solution has been evaluated with our VIE formulation (red continuous line) and with the null field method (red circles); the corresponding isotropic scenarios have also been solved with the VIE formulation (dashed black line). The slab has been excited by an x-polarized plane wave, propagating along the z- axis with wavelengths $\lambda = 5m$ (a),(b), and $\lambda = 1m$ (c),(d). ©2017 IEEE. Reprinted, with permission, from [8].

eralized eigenvalue problem, resulting from (9) and (10), with $\mathbf{R} = \mathbf{0}$:

$$\mathbf{D}\left(\omega_0\right)\mathbf{I} = \lambda \mathbf{L}\left(\omega_0\right)\mathbf{I}, \tag{18}$$

where ω_0 is th particular value of ω used for the computation of the matrices. Notice that, in this simple case, the facet shape functions are not needed and that the $i-th$ resonant frequency is given as:

$$f_i = \frac{1}{2\pi\sqrt{\lambda_i}} \tag{19}$$

The split ring here analysed is described in [3]. In [3], the authors report experimental, analytic and numerical results, so that this case can be chosen as a convenient benchmark for our numerical approach. The values of their geometrical parameters are $l = 5mm, r_{e1} = 11mm, r_{i1} = 10mm, r_{e2} = 7.5mm, r_{i2} = 6.7mm$, and $g = 1mm$, where l is the height of both cylinders, r_e and r_i are the external and internal radii and g is the width of the gaps. The current density distribution associated to the first two resonant modes computed by solving 18 are shown in 4, where also the mesh used in the computation is shown. The frequency of the first resonant mode ($f = 1.446GHz$) is in a very good agreement with the experimental value ($f_{exp} = 1.45GHz$ reported in [3]. Notice that there is a light dependence of the resonance frequency upon the frequency used for computing the L and D matrices. This behaviour is shown in Table 1. Finally, in Fig. 5, the squared magnitude of the electric field scattered from the slit-ring is shown. The field has been evaluated in the far zone along the z axis as a function of the frequency. In Fig. 5a, the slit-ring is excited by an $x-$polarized plane wave propagating along the $y-$ axis., while in 5b the excitation is given by a $y-$polarized plane wave, propagating along the $x-$ axis.

$f\,[GHz]$	$1st$ resonant frequency $[GHz]$	$2nd$ resonant frequency $[GHz]$
1.450	1.446	3.193
1.446	**1.446**	3.1926
3.275	1.399	3.280
3.280	1.399	**3.280**

Table 1: Resonant frequencies as a function of the frequency f where $\mathbf{L}$ and $\mathbf{D}$ matrices are computed

B Anisotropic dielectric slab

Next, we consider a uniaxial dielectric slab with equal length L and width W, i.e. $L = W = 2m$, and height $H = 1.2m$, featuring a relative permittivity tensor $\bar{\bar{\varepsilon}}_r = \text{diag}\,[2, 2, 5]$ in Cartesian coordinates. We used the hexahedral mesh shown in Fig. 6 (a), featuring 18432 elements, $N_L = 34689$ loop shape functions, $N_F = 18431$ facet shape functions and $N_S = 4351$ star shape functions, leading to 57471 complex unknowns. The slab is excited by an x-polarized plane wave propagating along the z axis, with wavelength $\lambda = 5m$ (size parameter $k_0 L = 2.5$) and $\lambda = 1m$ (size parameter $k_0 L = 12.6$), respectively.

Regarding the null field method computations, for the case of $\lambda = 5m$ we have assumed for the expansion of both the internal

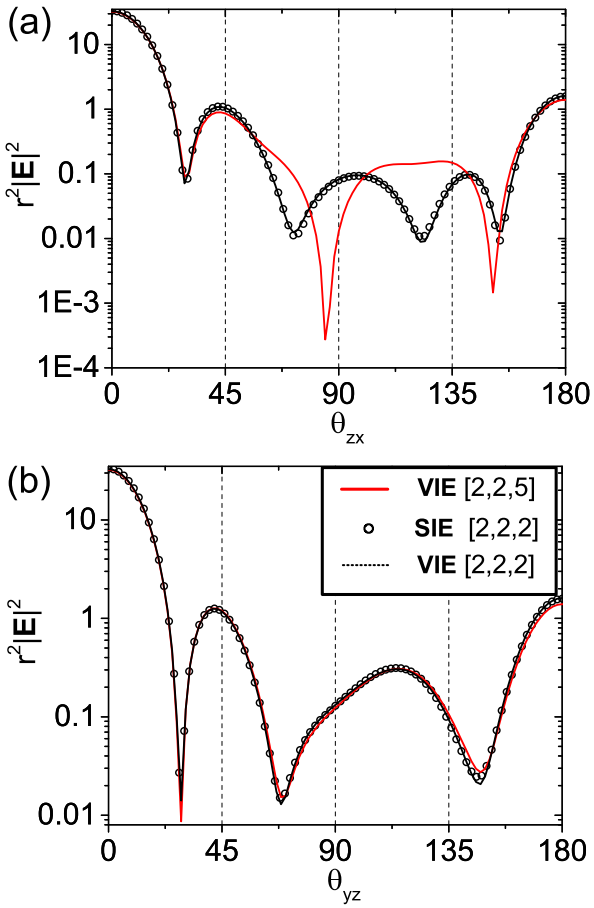

Figure 8: Squared magnitude of the electric field scattered from an anisotropic slab with equal length L and width W, i.e $L = W = 2m$, and height $H = 0.6m$ and with $\bar{\varepsilon}_r = \text{diag}\,[2, 2, 5]$, evaluated in the far zone as a function of the inclination angle θ in zx plane (a) and in the yz plane (b). The solution has been evaluated with our VIE formulation (red continuous line); the corresponding isotropic scenarios have also been solved with the SIE formulation (black squares) and with the VIE formulation (black continuous lines). The slab has been excited by an x-polarized plane wave, propagating along the z axis with wavelength $\lambda = 1m$. ©2017 IEEE. Reprinted, with permission, from [8]

and the incident field $N_{max} = 11$, while for the case of $\lambda = 1m$ we have assumed $N_{max} = 17$.

In Fig. 7 we show the squared magnitude of the scattered electric field computed in the far zone as a function of the inclination angle θ in the zx plane (a),(c) and in the yz plane (b),(d) assuming an incident wavelength of $\lambda = 5$m (a),(b) and of $\lambda = 1$m (c),(d), respectively. In particular, we plot with a continuous red line the results obtained with the presented VIE method, with red open circles the corresponding quantities obtained with the null field method, and with a black dashed line the solution for the corresponding isotropic case with $\bar{\varepsilon}_r = \text{diag}\,[2, 2, 2]$. Regarding the null-field calculations, we used the code developed by A. Doicu, T. Wriedt, and Y. Eremin [10], which, for the case of anisotropic particles, is based on the approach of Kiselev [9]. We found excellent agreement in all the investigated cases.

Finally, we have also carried out the same analysis for a slab with a higher aspect ratio. In this case, the height of the slab has been chosen as $H = 0.6m$, while we kept the length and width the same of the previous example, i.e. $L = W = 2$. The corresponding mesh is shown in 6 (b), featuring 18432 elements, $N_L = 34689$ loop shape functions, $N_F = 18431$ facet shape functions and $N_S = 4351$ star shape functions, leading to 57471 complex unknowns. In this case, due to the high aspect ratio of the object, the null field method breaks down since the matrix $\mathbf{Q}$ becomes ill-conditioned. Qualitatively, this is due to the fact that the vector quasi spherical wave functions are not suited to describe the morphology of the electromagnetic field in geometries that strongly deviate from a spherical one. Therefore, in Fig. 8, we only show the results obtained with our VIE formulation. For the sake of completeness, we show in the same figure also the solution of the isotropic case obtained with the VIE formulation and with the PMCHWT (Poggio-Miller-Chu-Harrington-Wu-Tsai) surface integral formulation implemented in Ref. [37].

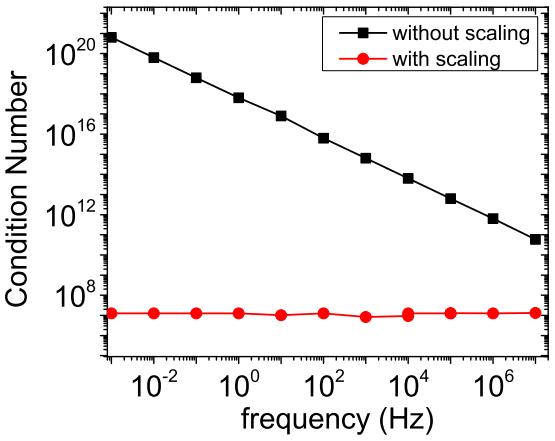

Figure 9: Condition number of the problem of a slab of dimensions $L = 50mm; W = 16mm; H = 3mm$ with conductivity tensor $\sigma = \text{diag}\left[10^4, 10^2, 10^2\right]$ excited by a magnetic dipole at frequency f, parallel to the z axis, and located at a vertical distance of $30mm$ from the upper face of the slab in correspondence of its center. ©2017 IEEE. Reprinted, with permission, from [8]

C Frequency stability

We now provide numerical evidence of the stability of our method over a broad frequency range by considering a slab of dimensions $L = 50mm$, $W = 16mm$, $H = 3mm$ exhibiting a conductivity tensor $\sigma = \text{diag}\left[10^4, 10^2, 10^2\right]$. The slab is excited by a magnetic dipole oscillating at frequency f, which is oriented parallel to the z axis, and located at a vertical distance of $30mm$ from the upper face of the slab, in correspondence of its center. We used a hexahedral mesh with 21087 elements, $N_L = 32785$ loop shape functions, $N_F = 17919$ facet shape functions and $N_S = 6111$ star shape functions, leading to 56815 complex unknowns. In Fig. 9 we show with a red line the condition number of the matrix $\tilde{\mathbf{Z}}$ of Eq. 16, scaled according to the prescriptions of Eq. 17, and with a black line the condition number of the unscaled problem. It is apparent that the performed scaling makes the condition number almost constant as we vary the frequency over ten orders of magnitude. We conclude that our VIE formulation, equipped with a suitable scaling of the loop, star and facet components, is stable over a wide range of frequencies. On the other hand, without the scaling, the condition number increases exponentially as we decrease the exciting frequency.

V Conclusions

In this work, we introduced a volume integral equation method for the solution of the electromagnetic scattering from an electrical anisotropic inhomogeneous object.

Excellent accuracy of the developed method has been found by comparing its outcomes against the experimental results in the case of a classic split-ring resonator of interest for the analysis of complex metamaterial design. Excellent agreement has been also found by comparing the results of the analysis against the null-field and SIE methods, for selected cases [8]. Tests on the electric field scattered in the near and far zone from a uniaxial electric sphere have been also already published in [8].

Our method, being intrinsically free from the low-frequency breakdown problem, shows numerical stability regardless of the frequency of the excitation, in contrast to other existing VIE approaches. Moreover, compared to the null field method, our approach does not suffer from ill-conditioned matrices that plague the latter method when the shape of the scatterer strongly deviates form a sphere. Finally, compared to surface integral equation approaches, our VIE formulation is not limited to piecewise homogeneous materials, but can also handle inhomogeneous anisotropic objects. We also point out that, similarly to any other volume integral approach, the application of the present implementation is limited to objects of size comparable to the wavelength due to its memory requirements and computational burden, unless suitable parallel sparsification techniques are used.

VI Acknowledgments

Some parts of this paper have been published in [8], ©2017 IEEE. Reprinted, with permission, from [8]. We would like to acknowledge the IEEE for the licence.

VII References

[1] A. E. Ruehli, "Equivalent circuit models for three dimentional multiconductor systems," *IEEE Trans. Microw. Theory Tech.*, vol 22, pp. 216–221, 1974.

[2] H. Heeb and A. E. Ruheli, "Three dimensional interconnect analysis using partial element equivalent circuits," *IEEE Trans. Circuits Syst. I, Fundam. Theory Appl.*, vol 39, pp. 974–982, 1992.

[3] A. Radkovskaya, M. Shamonin, C. J. Stevens, G. Faulkner,D. J. Edwards, E. Shamonina, and L. Solymar, "Resonant frequencies of a combination of split rings: experimental, analytical and numerical study," *Microwave and Optical Technology Letters*, Vol. 46, No. 5, pp. 473-475, Sept. 2005

[4] A. Poddubny, I. Iorsh, P. Belov, and Y. Kivshar, "Hyperbolic metamaterials," *Nature Photonics*, vol. 7, no. 12, pp. 948–957, 2013.

[5] J. B. Pendry, D. Schurig, and D. R. Smith, "Controlling electromagnetic fields," *Science*, vol. 312, no. 5781, pp. 1780–1782, 2006.

[6] U. Leonhardt, "Optical conformal mapping," *Science*, vol. 312, no. 5781, pp. 1777–1780, 2006.

[7] C. Qiu, L. Gao, J. D. Joannopoulos, and M. Soljačić, "Light scattering from anisotropic particles: propagation, localization, and nonlinearity," *Laser & Photonics Reviews*, vol. 4, no. 2, pp. 268–282, 2010.

[8] C. Forestiere, G. Miano, G. Rubinacci, A. Tamburrino, L. Udpa, and S. Ventre, "A Frequency Stable Volume Integral Equation Method for Anisotropic Scatterers," *IEEE Transactions on Antennas and Propagation*, vol. 65, pp. 1224–1235, March 2017.

[9] A. Kiselev, V. Y. Reshetnyak, and T. Sluckin, "Light scattering by optically anisotropic scatterers: T-matrix theory for radial and uniform anisotropies," *Physical Review E*, vol. 65, no. 5, p. 056609, 2002.

[10] A. Doicu, T. Wriedt, and Y. Eremin, *Light Scattering by Systems of Particles*. Springer-Verlag, 2006.

[11] A. Taflove and K. R. Umashankar, "Analytical models for electromagnetic scattering," Tech. Rep. Final Report RADC-TR-85-87, Contract F19628-82-C-0140, MA, Rome Air Development Center, Hanscom Air Force Base (AFB), 1985.

[12] B. Beker, K. R. Umashankar, and A. Taflove, "Numerical analysis and validation of the combined field surface integral equations for electromagnetic scattering by arbitrary shaped two-dimensional anisotropic objects," *Antennas and Propagation, IEEE Transactions on*, vol. 37, no. 12, pp. 1573–1581, 1989.

[13] M. A. Strickel and A. Taflove, "Time-domain synthesis of broad-band absorptive coatings for two-dimensional conducting targets," *Antennas and Propagation, IEEE Transactions on*, vol. 38, no. 7, pp. 1084–1091, 1990.

[14] J. Schneider and S. Hudson, "A finite-difference time-domain method applied to anisotropic material," *IEEE Transactions on Antennas and Propagation*, vol. 41, pp. 994–999, Jul 1993.

[15] K. Yee and J. Chen, "The finite-difference time-domain (FDTD) and the finite-volume time-domain (FVTD) methods in solving maxwell's equations," *Antennas and Propagation, IEEE Transactions on*, vol. 45, pp. 354–363, mar 1997.

[16] G. Mumcu, K. Sertel, and J. L. Volakis, "Surface integral equation solutions for modeling 3-d uniaxial media using closed-form dyadic green's functions," *IEEE Transactions on Antennas and Propagation*, vol. 56, pp. 2381–2388, Aug 2008.

[17] R. Graglia and P. Uslenghi, "Electromagnetic scattering from anisotropic materials, part i: General theory," *Antennas and Propagation, IEEE Transactions on*, vol. 32, no. 8, pp. 867–869, 1984.

[18] R. Graglia and P. Uslenghi, "Electromagnetic scattering from anisotropic materials, part ii: computer code and numerical results in two dimensions," *Antennas and Propagation, IEEE Transactions on*, vol. 35, no. 2, pp. 225–232, 1987.

[19] R. D. Graglia, P. L. Uslenghi, and R. S. Zich, "Moment method with isoparametric elements for three-dimensional anisotropic scatterers," *Proceedings of the IEEE*, vol. 77, no. 5, pp. 750–760, 1989.

[20] V. V. Varadan, A., and V. K. Varadan, "Scattering by three-dimensional anisotropic scatterers," *IEEE Transactions on Antennas and Propagation*, vol. 37, pp. 800–802, Jun 1989.

[21] A. Lakhtakia, "General theory of the purcell-pennypacker scattering approach and its extension to bianisotropic scatterers," *The Astrophysical Journal*, vol. 394, pp. 494–499, 1992.

[22] B. T. Draine and P. J. Flatau, "User guide for the discrete dipole approximation code ddscat 7.3," *arXiv preprint arXiv:1305.6497*, 2013.

[23] G. Kobidze and B. Shanker, "Integral equation based analysis of scattering from 3-d inhomogeneous anisotropic bodies," *Antennas and Propagation, IEEE Transactions on*, vol. 52, no. 10, pp. 2650–2658, 2004.

[24] J. Markkanen, P. Yla-Oijala, and A. Sihvola, "Discretization of volume integral equation formulations for extremely anisotropic materials," *Antennas and Propagation, IEEE Transactions on*, vol. 60, no. 11, pp. 5195–5202, 2012.

[25] M. S. Tong, Y. Q. Zhang, R. P. Chen, and C. X. Yang, "Fast solutions of volume integral equations for electromagnetic scattering by large highly anisotropic objects," *Microwave Theory and Techniques, IEEE Transactions on*, vol. 62, no. 7, pp. 1429–1436, 2014.

[26] L. E. Sun, "Computations of electromagnetic wave scattering from anisotropic and inhomogeneous objects using volume integral equation methods," in *2015 IEEE International Symposium on Antennas and Propagation USNC/URSI National Radio Science Meeting*, pp. 1820–1821, July 2015.

[27] L. E. Sun and W. C. Chew "Modeling of Anisotropic Magnetic Objects by Volume Integral Equation Methods," in *Applied Computational Electromagnetics Society Journal*, vol. 30, no. 12, pp. 1256–1261, 2015.

[28] R. Albanese and G. Rubinacci, "Solution of three dimensional eddy current problems by integral and differential methods," *IEEE Transactions on Magnetics*, vol. 24, pp. 98–101, Jan 1988.

[29] R. Albanese and G. Rubinacci, "Finite element methods for the solution of 3d eddy current problems," vol. 102 of *Advances in Imaging and Electron Physics*, pp. 1 – 86, Elsevier, 1997.

[30] J.-S. Zhao, and W. C. Chew, "Integral equation solution of Maxwell's equations from zero frequency to microwave frequencies," *IEEE Transactions on Antennas and Propagation*, vol. 48, pp. 1635–1645, Oct 2000.

[31] G. Rubinacci and A. Tamburrino, "A broadband volume integral formulation based on edge-elements for full-wave analysis of lossy interconnects," *IEEE Transactions on Antennas and Propagation*, vol. 54, pp. 2977–2989, Oct 2006.

[32] A. Bossavit, *Computational electromagnetism: Variational formulations, Edge elements, Complementarity*. Academic Press, 1998.

[33] G. Miano, G. Rubinacci, A. Tamburrino, and F. Villone, "Linearized fluid model for plasmon oscillations in metallic nanoparticles," *IEEE Transactions on Magnetics*, vol. 44, pp. 822–825, June 2008.

[34] G. Miano, G. Rubinacci, and A. Tamburrino, "Numerical modeling for the analysis of plasmon oscillations in metallic nanoparticles," *IEEE Transactions on Antennas and Propagation*, vol. 58, pp. 2920–2933, Sept 2010.

[35] J. B. Pendry, A. J. Holden, D. J. Robbins, and W. J. Stewart, "Magnetism from conductors and enhanced nonlinear phenomena," *IEEE Trans. Microw. Theory Tech.*, vol. 47, pp. 2075-2084, 1999.

[36] G. Miano, and F. Villone, "A surface integral formulation of Maxwell equations for topologically complex conducting domains," *IEEE Transactions on Antennas and Propagation*, vol. 53, pp. 4001-4014, 2005.

[37] C. Forestiere, G. Iadarola, G. Rubinacci, A. Tamburrino, L. Dal Negro, and G. Miano, "Surface integral formulations for the design of plasmonic nanostructures," *J. Opt. Soc. Am. A*, vol. 29, pp. 2314–2327, Nov 2012.

AUTHORS NAME AND AFFILIATION

Carlo Forestiere, Giovanni Miano and Guglielmo Rubinacci, Department of Electrical Engineering and Information Technology, Università degli Studi di Napoli Federico II, via Claudio 21, Napoli, 80125, Italy.

forestiere@unina.it, miano@unina.it, rubinacci@unina.it

Antonello Tamburrino and Salvatore Ventre, Department of Electrical and Information Engineering, Università di Cassino e del Lazio Meridionale, Cassino, Italy.

tamburrino@unicas.it, ventre@unicas.it

Lalita Udpa, Department of Electrical and Computer Engineering, Michigan State University, East Lansing, MI 48824 USA

udpal@egr.msu.edu

Antonello Tamburrino is also with the Department of Electrical and Computer Engineering, Michigan State University, East Lansing, MI 48824 USA